

Electron cyclotron heating and current drive in the TJ-II stellarator

V Tribaldos†, J A Jiménez, J Guasp and B Ph van Milligen

Asociación EURATOM-CIEMAT para Fusión, Avenida Complutense 22, Madrid 28040, Spain

Received 25 November 1997, in final form 1 September 1998

Abstract. Electron cyclotron resonance heating (ECRH) has become an attractive technique in today's fusion experiments not only as a heating mechanism but also as a diagnostic tool and a way to induce controllable currents through electron cyclotron current drive (ECCD). In this paper we show, using ray tracing simulations, how one can address all these issues with the ECRH system designed for the TJ-II stellarator. This ECRH set up consists of two 500 kW gyrotrons at $f = 53.2$ GHz coupled to the plasma through two quasi-optical transmission lines, placed at two stellarator symmetric positions, and equipped with an internal steerable mirror. Using the three-dimensional (3D) Hamiltonian ray tracing code, TRECE, almost full single-pass absorption with localized power deposition is found for both on- and off-axis heating for any magnetic configuration. The simulations also show that it is possible to induce an appreciable ECCD despite the small oblique incidence angles attainable with the movable mirrors because of the rapid variation of the magnetic field direction and strength with the toroidal angle in TJ-II.

1. Introduction

The design of the electron cyclotron resonance heating (ECRH) system for a fusion device, apart from engineering considerations, mainly involves the optimization of the launching position and orientations to obtain maximum single-pass absorption, maximum power deposition and a narrow deposition profile. Moreover, since in today's experiments ECRH is also often used as a diagnostic tool well designed ECRH system has to comply with requirements like being able to deposit the power on- and off-axis and to induce controllable currents. However, these additional requisites impose even more constraints on the optimization procedure. The solution of this optimization problem is very sensitive to the spatial distribution of the magnetic field modulus. In devices where the spatial variation of the magnetic field strength is dominated by toroidal symmetry, such as tokamaks, the optimization is more straightforward than in devices where such symmetry is absent and all the components of the magnetic field are of the same magnitude. The TJ-II stellarator is a typical example of a fully three-dimensional (3D) magnetic field.

From the point of view of ECRH the main differences between the TJ-II stellarator and other classical stellarators or torsatrons are: a large helical axis excursion of the plasma, of approximately 25 cm, which in most other devices is only a few centimetres; the magnetic field mode structure, richer than in most other devices: TJ-II needs, at least, 15 B_{mn} modes, in Boozer coordinates, to describe the main characteristics of B ; the flexibility of the magnetic configuration, that translate into rather large changes in the plasma position, shape and size.

† To whom correspondence should be addressed.

The purpose of this study is to show how one can meet all of the requirements that are usually achieved with ECRH in other fusion devices, in the complex geometry of TJ-II. Those requirements include changing the power deposition from on- to off-axis and the possibility to induce appreciable currents in both directions. The latter is especially important for shearless devices like TJ-II in order to control the rotational transform profile.

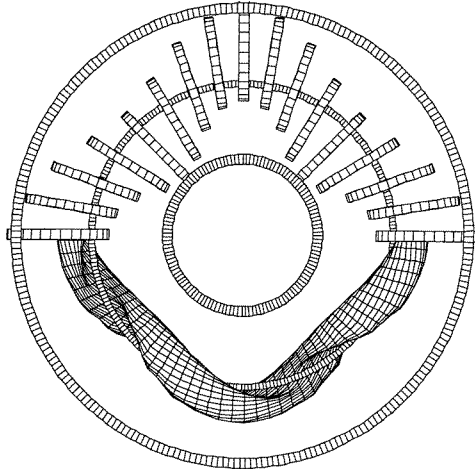


Figure 1. Top view of the coil configuration and plasma of the TJ-II stellarator.

The paper is organized as follows. In section 2 some aspects about the TJ-II stellarator and its peculiarities are summarized along with the actual design of the ECRH system; 3D Hamiltonian ray tracing calculations are presented in section 3 for the power deposition profiles and the induced currents, also in this section the performance and limitations of the ECRH set up are highlighted; and finally conclusions will be drawn in section 4.

2. TJ-II stellarator

TJ-II is a mid-size four period helical axis stellarator, see [1], that has recently started operation at CIEMAT, in Madrid, Spain. The magnetic field of TJ-II (1 Tesla) is obtained with the set of coils of figures 1 and 2 (to give an idea of the size of the device the diameter of the outer vertical field coils is 4.6 m). The helically positioned toroidal coils together with its two central conductors, one circular and one helical (with the same winding law as the toroidal coils) gives TJ-II the possibility to access a wide range of magnetic configurations by changing the currents flowing through the central conductors. This flexibility permits rotational transform between 0.9 and 2.5, magnetic shear between -1 and 10% and magnetic well depths between 0 and 6% almost independently, and also makes the plasma position shape and size different from configuration to configuration. Before starting the discussion on the ECRH system it is necessary to briefly describe some of the main differences between other classical stellarators and torsatrons and TJ-II. As has been noted in the introduction, the helical structure of the plasma is one of the most complex issues, because it depends more on the device's geometry than in the detailed magnetic configuration used. The plasma swings around the central conductors ($R_0 = 1.5$ m), i.e. for the standard configuration the

position of the axis is 1.73 m for toroidal angle $\varphi = 0^\circ$ and 1.29 m for $\varphi = 45^\circ$, thus giving an helical axis excursion is of approximately 25 cm.

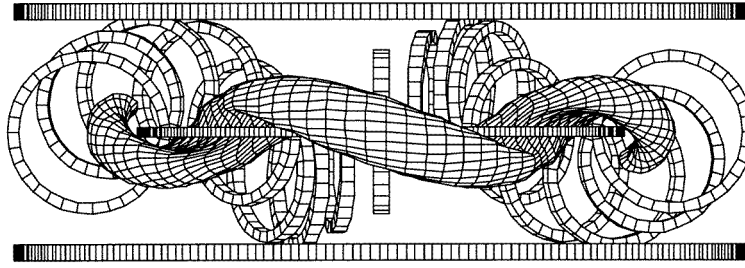


Figure 2. Side view of the coil configuration and plasma of the TJ-II stellarator.

In figure 3 constant toroidal normalized magnetic flux, ψ , and the magnetic field modulus are shown for $\varphi = 4.72^\circ, 14.52^\circ, 25.47^\circ$ and 38.17° along with the vacuum vessel. Since there are eight sectors per period of the device, named A, B, C and D, these are all the possible window ports because of the periodicity and stellarator symmetry.

Because the configuration space available for TJ-II is mainly obtained by changing the currents flowing through the central circular and helical coils, and the field created by these coils is relatively small compared with the one produced by the helically positioned toroidal coils, the mod B structure of figure 3 remains almost unchanged, and only the shape, size and position of the plasma is modified from configuration to configuration. However, since the plasma position and size depends on the configuration, the ripple of the magnetic field at a given magnetic surface can be quite different from configuration to configuration. This is the reason we have selected three configurations from geometrical considerations, and choose one large, very indented plasma (fat), a standard plasma (std), and one small nearly elliptical plasma. For simplicity these are the same configurations used in [2], and their main parameters are described in table 1. For TJ-II the common definition of minor radius is misleading because the plasma cross section is bean-shaped. Here we have adopted the definition for the minor radius, a , to be the radius of an equivalent circular tokamak with the same major radius and having the same plasma volume, thus, for example, for the standard configuration having 1 m^3 of plasma the minor radius is $a = 0.1837 \text{ m}$, and then by definition $r = ar_{\text{eff}} \equiv a\sqrt{\psi}$.

Table 1. TJ-II configurations used throughout this paper.

Configurations	ϵ	Plasma volume (m^3)	a (cm)
Fat	1.91	1.1654	21
Std	1.46	0.9848	18
Low	1.01	0.2315	9

From the point of view of ECRH there are several constraints for the launching set up. The system must be capable, at least, to heat every magnetic configuration on- and off-axis without inducing any current by electron cyclotron current drive (ECCD), and also to induce currents on- and off-axis, and to deposit the power at positions with different fractions of trapped particles. To fulfil all these requirements, to minimize the refraction effects and

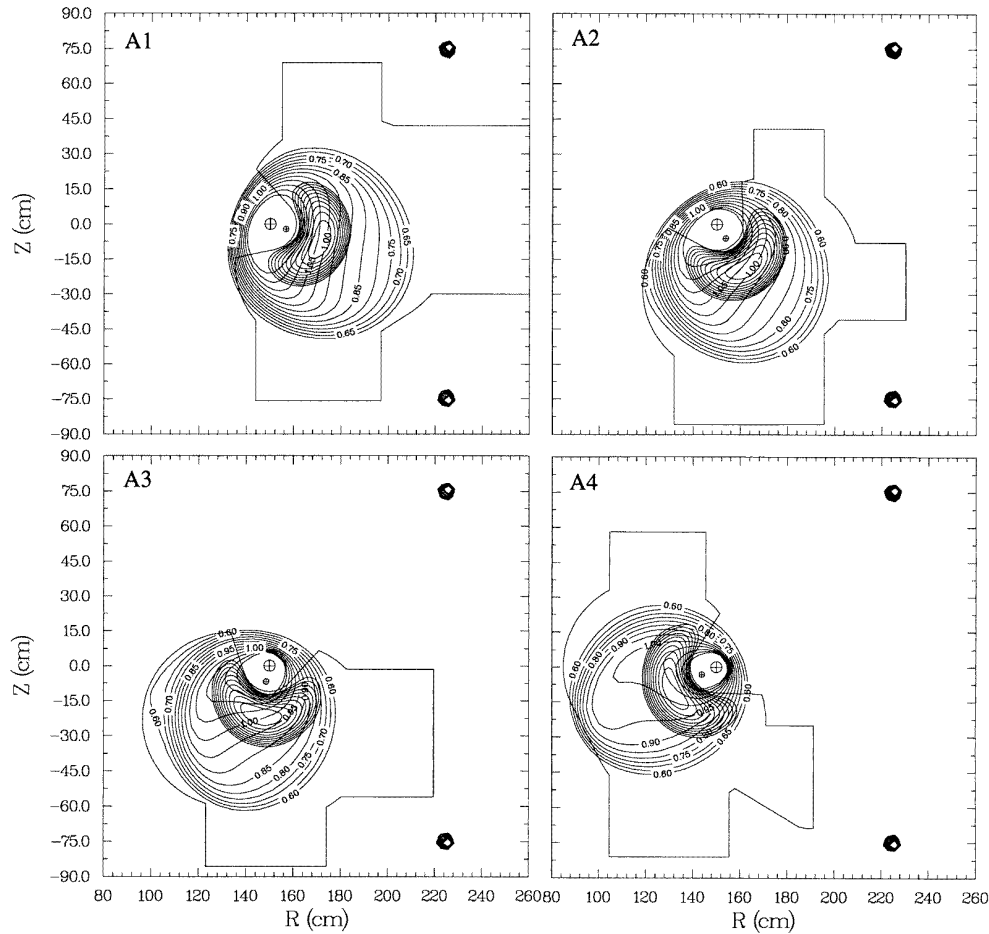


Figure 3. Level curves of constant flux, and magnetic field modulus for the standard configuration of TJ-II for the sectors (A1) $\varphi = 4.72^\circ$; (A2) $\varphi = 14.52^\circ$; (A3) $\varphi = 25.47^\circ$; and (A4) $\varphi = 38.17^\circ$.

obtain a narrow deposition profile, it is desirable to have a line sight in the direction of maximum density gradient and being as perpendicular as possible to the resonant magnetic field. Here arise two difficulties: due to the helicity of the plasma, only a small portion of the plasma is accessible for many of the vacuum vessel windows (except for some special tangential windows that will be used for neutral beam injection (NBI)); and the strong dependence of the mod B contours on the toroidal angle, see figure 3. Thus, the launching system would provide a way to direct the microwaves to different toroidal and poloidal positions. Using these criteria, the most suitable injection planes are those corresponding to the first and third sectors. In the second sector (A2 in figure 3), due to the reduced size of the three windows there is a lack of space for placing a mirror, and in the fourth sector the angle that the density gradient makes with the constant magnetic field lines is very large.

To choose between the first and third sectors we can use two facts: the lower absorption in the A1 sector for low densities and temperatures because its magnetic field gradient is larger in sector A3; the toroidal dependence of the magnetic field that, in the end, is related

with the coil structure, and translates into a very broad mod B spectrum, see figure 4. The implications of this structure on ECRH are the accessibility and the fraction of trapped particles. However, the distribution of trapped particles in TJ-II has a very complex structure. In figure 5, curves of constant fraction of trapped particles, $(1 - B/B_M)^{1/2}$, are shown for the configurations of table 1 and three radial positions, as a function of the toroidal and poloidal angles. From this plot is it apparent that TJ-II has a very large fraction of trapped particles (as large as 60%), that this fraction increases with the effective radius, the minor radius of the configuration a and that the maximum and minimum positions depend weakly on the configuration. Comparing figures 3 and 5, taking into account that $\theta = 0$ points in the direction of increasing major radius, the position of the maximum fraction of trapped particles is located near the fourth sector (in figure 3(d)). In computing the fraction of trapped particles, it is assumed that particles do not depart appreciably from the field lines, i.e. no drifts are considered. Thus, the calculations only include geometrical factors, and no dynamical effects. To check this assumption, a code [3] has been used that follows the particle orbits in Boozer coordinates, using the guiding centre approximation and neglecting collisions. The code was run following 30720 particles (electrons or ions) with starting conditions corresponding to 32 toroidal angles (in one machine period) 24 poloidal angles and 40 pitch angles (uniformly distributed in spatial angles and pitch angles). A particle is considered to be trapped if in its evolution it changes the sign of its pitch angle. A typical run of the code takes approximately 1.5 h dedicated time, using 16 processors of a CRAY-T3E for one magnetic surface, electric potential and energy, of a given magnetic configuration. Since no collisions are included, the results obtained for the fraction of trapped particles using this code can only be regarded as an upper bound for this fraction.

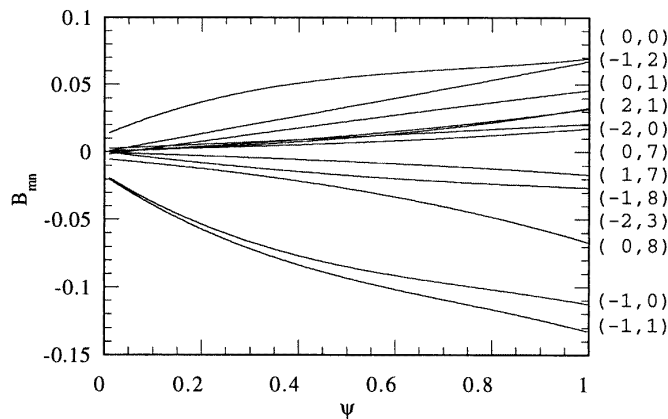


Figure 4. Dependence of Fourier harmonics, in Boozer co-ordinates, with the normalized magnetic flux ψ , for the standard configuration of TJ-II. Selected modes are at least 1/50 of the dominant mode for any ψ .

As a general result, estimating the fraction of trapped particles with $(1 - B/B_M)^{1/2}$ seems to be a good approximation for electrons and an underestimation for ions near the axis, and the disagreement between both results is found to increase with the particles' energy. In figure 6 we present a comparison between the average fraction of trapped particles against the effective radius, computed as in figure 5 and with this code for electrons and ions (both with $E = 500$ eV). This result also holds for other configurations and, as stated previously, its absolute value mainly depends on the minor radius, a , of the configuration.

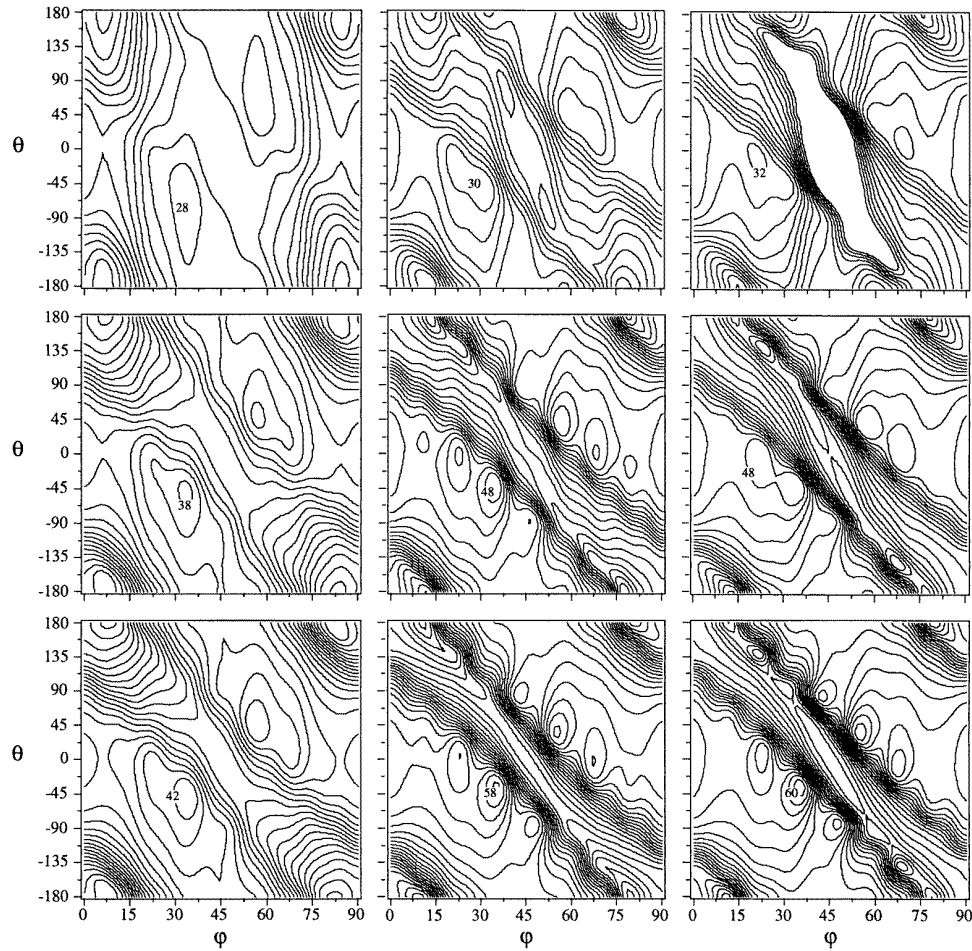


Figure 5. Level curves of constant fraction of trapped particles against the toroidal, φ , and poloidal, θ , angles for: from left to right low, std and fat configurations, and from top to bottom $r_{\text{eff}} = 0.3, 0.5$ and 0.77 . Contour lines are separated by 2%.

Thus, when considering ECCD, we will compute the fraction of trapped particles using $(1 - B/B_M)^{1/2}$. The large fraction of trapped particles found, together with their strong toroidal and poloidal dependences can influence the plasma performance profoundly during the first experimental campaigns in TJ-II, since only ECRH will be used for heating. To treat the kinetic effects self-consistently, it is necessary to consider not only the distribution function of passing electrons but also the different distribution functions corresponding to the different magnetic field ripples, and treat their mutual interaction through collisions with the microwave beam and introduce some power sink in phase space due to convective losses. In the W7-AS [4] stellarator this type of treatment has been used: a bounce averaged Fokker–Planck equation near the axis has been solved, taking into account only one magnetic field ripple component for different heating power densities and heating scenarios (X- and O-modes). The result obtained for W7-AS cannot be directly applied to TJ-II because of the importance of several magnetic ripple components even near the axis, see figure 5; the high-

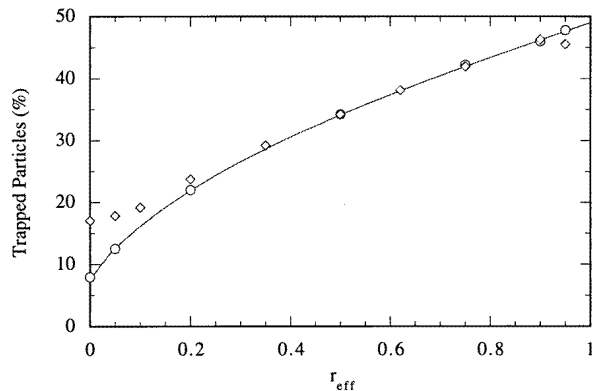


Figure 6. Average fraction of trapped particles, against the effective radius, r_{eff} , for the standard configuration of TJ-II, using the relation $(1 - B/B_M)^{1/2}$ (solid), and the results of the code for electrons (○) and ions (◇).

power densities expected, see section 3.1; and the rapid particle and energy losses in the long mean free path collisionality regime, even for moderate radial electric field. However, some of the qualitative conclusions of this work can be applied for on-axis heating in TJ-II, namely: a degradation in the heating efficiency due to a *quasi-linear* deformation of the electron distribution function and a broadening in the power deposition profile because of the radial transport of locally trapped suprathermal electrons.

Using these arguments it seems more interesting, for the investigation of the possible effects of trapped particles, to choose sector A3, corresponding to $\varphi = 25.47^\circ$, for injection, since here the relative change in this fraction is maximum.

2.1. The ECRH system of TJ-II

The basic ECRH system consists of two 500 kW gyrotrons at $f = 53.2$ GHz (second harmonic for the TJ-II field) and a pulse length of 1 s. These gyrotrons are coupled to the plasma with two quasi-optical transmission lines [5] with an estimated transmission coefficient of 0.9. The lines are located at two toroidal stellarator symmetric positions (the stellarator symmetry for TJ-II is such that $\psi(R, \pi/4 + \varphi, z) = \psi(R, \pi/4 - \varphi, -z)$). The first line QTL1 launches the microwaves through the side window of the B3 sector of TJ-II (at $\varphi = 25.47^\circ$) whereas the second line QTL2 uses the side port of the A6 sector (at $\varphi = 64.53^\circ$). Both lines use a set of eight external mirrors (six cylindrical mirrors coupled in pairs and two elliptical mirrors) plus one steerable elliptical mirror located inside the vacuum vessel. The internal mirror of each line can rotate through an angle a_1 in the toroidal direction from -10° to 10° (with respect to the injection plane) and through an angle a_2 , in the poloidal direction from $0^\circ < a_2 < 35^\circ$ (with respect to the z axis), giving a beam waist near the beam axis of approximately 1 cm. The beams of both lines are launched from the low-field side. The limitations of the mirror movements are mainly due to the lack of space inside the vacuum chamber and the helical structure of the plasma. It should be noted that although the mirror movement is small, especially in the toroidal direction, the angle between the magnetic field \mathbf{B} and the wavevector \mathbf{k} , which determine the parallel refractive index $N_{\parallel} = (c/\omega|\mathbf{B}|)\mathbf{k} \cdot \mathbf{B}$, is considerably larger due to the strong dependence of the magnetic field on the toroidal and poloidal angles in TJ-II.

Another issue, not usually relevant for other fusion devices, that is discussed in this work is microwave polarization evolution inside the plasma. Usually the state of polarization of the EC waves that are launched for heating is chosen to be equal to the local polarization of the desired mode (ordinary or extraordinary) in the resonant position, discarding the possible change of polarization inside the plasma due to Faraday rotation or the coupling of the O- and X-modes due to the magnetic field shear. However, the strong dependence of the magnetic field on the toroidal angle together with the high local magnetic field shear prompted a study in TJ-II presented as an appendix.

Since the injection systems are located at two stellarator symmetric positions through the rest of the paper we will consider only the first line QTL1.

3. Ray tracing calculations

To analyse the performance of the ECRH system of TJ-II, extensive ray tracing calculations have been performed using the TRECE code [2] using the real geometry of the launching set up and taking into account the structure of the microwave beam. A limitation of the calculations presented here, is the assumption that the Gaussian shape of the real beam can be described within the framework of geometric optics. To model the Gaussian beam, a bunch of parallel rays is launched with a power distribution in the direction perpendicular to the propagation of $P(r) = P(0) \exp[-(r/w)^2]$, $0 < r < r_{\max}$. The parameters r_{\max} and w were chosen so as to give the same beam waist in vacuum as the real beam.

In the TRECE code the ray tracing equations are solved in Cartesian coordinates using a Runge–Kutta method of fourth order. The absorption coefficient is computed at each point of the calculated ray path using the weakly relativistic approximation for the Hermitian part, and the fully relativistic expressions for the anti-Hermitian part of the dielectric tensor, retaining all Larmor radius effects. Examples of the ray tracing trajectories are shown in figures 7 and 8 for $a_1 = -3.41^\circ$ and $a_2 = 30.02^\circ$ and the std configuration.

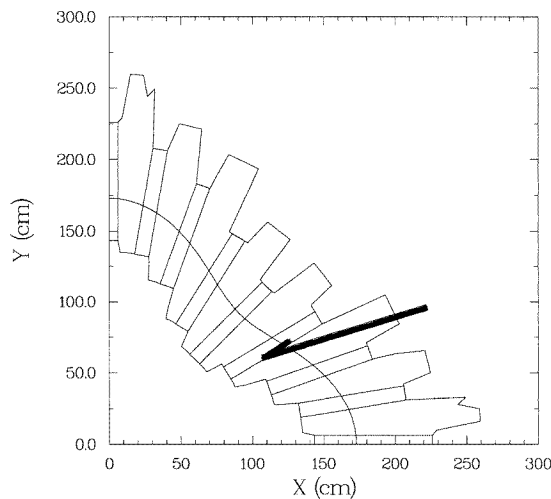


Figure 7. Top view of the vacuum vessel of TJ-II and the ray trajectories for the line QTL1.

Since in this work we are mainly concerned with general dependences and figures of merit rather than trying to give accurate estimations to compute the current driven by EC waves (ECCD), a linear estimate [6] has been used to obtain the response function by averaging Langevin equations, in the high-speed limit [7], but retaining trapped particle

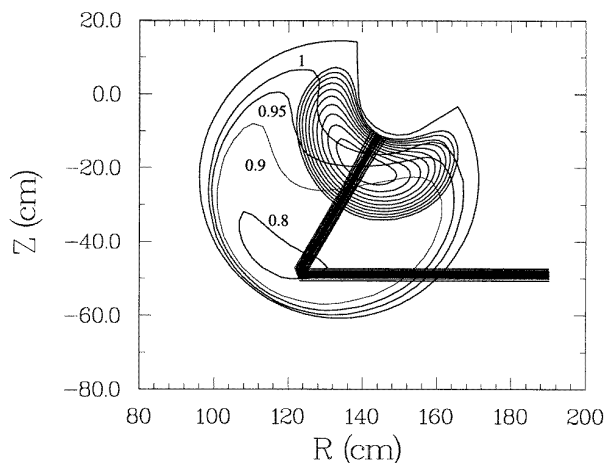


Figure 8. Projection of the ray trajectories in the toroidal plane $\varphi = 29.71^\circ$ with the magnetic flux surfaces, the magnetic field modulus (labelled in Tesla) and the vacuum vessel for the line QTL1. Notice that although the microwaves are injected by the A3 sector (see figure 7), because of the mirror the absorption takes place in a position between the coils.

effects. This approximation is not fully justified for the typical conditions of current drive by EC waves, where usually the velocity of the resonant electrons is not much larger than the thermal velocity ($v_R \approx 2 - 3v_{th}$) however, it contains all the essential features of the physical process, trapped particle effects can be included very easily and is equivalent to the more common adjoint approach [8]. The main drawback of the method is that it overestimates the contribution to the current of low velocity resonant electrons because it assumes a collision frequency smaller than its real collision frequency, and thus underestimates the rate at which current is destroyed by collisions. To estimate the error due to the low velocity resonant electrons we have included in table 2 the current induced neglecting the contribution of the resonant electrons with velocities smaller than $2.5v_{th}$.

Table 2. Comparison between total induced currents, in kA, with and without considering trapped particles, and neglecting the contribution from electrons with resonant velocities smaller than $2.5v_{th}$. This table refers to the conditions of figure 16.

Configurations	Case 1			Case 2		
	Trapped		Not trapped, no cut-off	Trapped		Not trapped, no cut-off
	No cut-off	$2.5v_{th}$		No cut-off	$2.5v_{th}$	
Std	1.55	1.14	2.02	3.91	2.32	4.64
Fat	1.61	1.17	1.86	4.14	2.99	5.40
Low	1.02	0.64	1.62	-2.27	-1.19	-3.43

The main difference between the results presented in this paper and those obtained in earlier studies of heating efficiency and current drive in TJ-II (cf [6]) is that here the real geometry of the launching systems is taken into account whereas in [6] only a numerical proof of principle was given, without including the geometric and practical considerations. however, it has been checked that both results agree for the conditions of [6].

The density and temperature profiles used are

$$n_e = n_e^0 (1 - \psi^{1.375})^{1.5} \quad T_e = T_e^0 (1 - \psi^{1.125})^{1.25}. \quad (1)$$

The dependence of ψ on the Cartesian co-ordinates is obtained from a neutral network fit [9], and the magnetic field is computed using the Biot–Savart law. Inside the ray tracing code also a density pedestal is assumed in order not to have a very steep density gradient in solving the ray equations, and thus not to violate the WKB approximation.

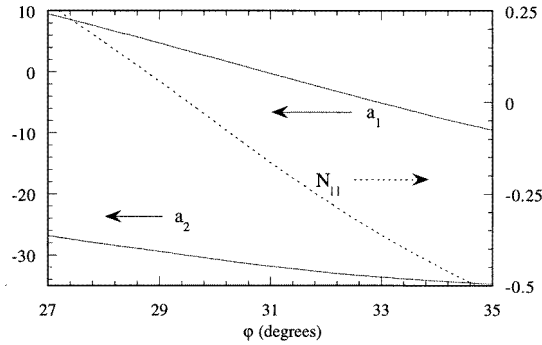


Figure 9. Toroidal, a_1 , and poloidal, a_2 , angles of the QTL1 steerable mirror with the parallel refractive index $N_{||}$ against the toroidal angle φ for the standard configurations of TJ-II.

Although for the high-power densities expected in TJ-II, quasi-linear deformations of the electron distribution function may play an important role throughout all simulations presented here, only Maxwellian electron distribution functions have been considered. However, since there are theoretical predictions and experimental evidence (cf [4]), that the power deposition profile is widened by deviations from the Maxwellian, one should regard the results that will be presented in section 3.1 and section 3.2 as lower bounds for the power deposition width and the induced current. Furthermore, the effect of the beam self-diffraction [10] can also lead to broader deposition profiles, lower power densities and a different non-inductive current drive for the real Gaussian beam that will be used for injection in TJ-II.

As has been noted, only three different plasma configurations (*fat*, *std* and *low*), representative of TJ-II (cf table 1 and figure 2 of [2]) were selected to show the performance of the ECRH. To accurately describe the launching conditions it is necessary to compute the toroidal (a_1) and poloidal (a_2) free angles of the mirror that ensure that the central ray of the beam hits the desired plasma position. This is done using the fact that the initial launching point and the plasma position, for a given magnetic configuration of the device are known, and that after a reflection only the sign of the wavevector component perpendicular to the plane defining the mirror has to be inverted. The actual situation for the TJ-II internal mirror is a little bit more complicated since the mirror position also depends on the mirror angles, but this degree of freedom is also incorporated in the calculation. In figure 9 the two angles of the mirror, a_1 and a_2 , and the parallel refractive index $N_{||}$ are shown for the standard configuration of TJ-II for on-axis launching at different toroidal positions, assuming straight line propagation (without including refraction due to the plasma). To be consistent with the use of parallel rays, and to avoid that the rays cross in the focal point, a plane mirror has been considered in this computation. This approximation is justified since the beam waist, calculated from the classical expressions for the Gaussian beam propagation in vacuum [11], is found to vary smoothly inside the plasma.

For the ray tracing simulations a bunch of 197 rays was launched with $r_{\max} = 2$ cm, $w = 1$ cm and $P_{\text{ECRH}} = 200$ kW for two different plasma densities and temperatures, one with moderate values (case 1) $n_e^0 = 1 \times 10^{19} \text{ m}^{-3}$, $T_e^0 = 0.5$ eV, used to set a lower bound for the single-pass absorption, and one with higher values (case 2) $n_e^0 = 1.5 \times 10^{19} \text{ m}^{-3}$, $T_e^0 = 1$ keV. For each plasma condition two different situations will be considered for the launching: a scan in the mirror angles so as to have approximately on-axis deposition at different toroidal positions; and a scan in the poloidal direction at a fixed toroidal angle. The dependence of the ECRH single-pass absorption and power deposition profiles on the magnetic configuration will be discussed in section 3.1 where it will be shown that the system is capable of localized on- and off-axis power deposition; the ECCD efficiency will be presented in section 3.2.

3.1. ECRH power deposition

Using the flexibility that the mirror movement allows, it is possible to heat the plasma on- and off-axis at different toroidal angles. We will first consider a scan in the mirror angles so as to have on-axis heating at different toroidal positions, thus with different N_{\parallel} . In figure 10 the position of the maximum in the power deposition profile is plotted against the toroidal angle at which the maximum absorption takes place for all the configurations and both density and temperature cases. Since the single-pass absorption exceeds 90%, even for the conditions of case 1, we can conclude that with this set up it is possible to have good on-axis absorption for every magnetic configuration of TJ-II even for low densities and temperatures. The results for this scan in the power deposition profile shows that within the flexibility of the steerable mirror it is possible to have on-axis deposition from 27° to 35° . Because the mirror angles have been chosen assuming straight line propagation, thus neglecting refraction effects, the maximum of the power deposition profile is not located on-axis for all the toroidal angles. This is also the reason why the curves for case 2 in figure 10 are more off-axis than those corresponding to case 1. However, the flexibility in choosing the mirror angles allows for correcting this refraction effect and optimize the launching for a known density profile, in order to have on-axis heating for every toroidal angle.

The complete power deposition profiles for special cases, of figure 10, in which the average parallel refractive index is close to zero, so that no current is induced by ECCD, appear in figure 11. Fixing the toroidal angle of the mirror to the values of figure 11 for each configuration, it is possible to have off-axis deposition by varying the poloidal angle of the mirror. The position where the maximum of the power deposition profile takes place is presented in figure 12, where the numbers indicate case 1 or case 2 conditions.

3.2. ECCD efficiency

We will make use of the launching flexibility to show that the designed ECRH system of TJ-II is also capable of inducing localized currents (this is particularly interesting for compensating bootstrap currents and controlling the rotational transform profile, ι). The plasma parameters we have considered for the simulations are the same as in section 3.1, and $Z_{\text{eff}} = 1$. In the calculations shown later, two different scans in the free angles of the mirror were considered: a scan in the angles so as to have on-axis absorption at different toroidal positions of the device, the same as in section 3.1; and a scan in the poloidal direction at a fixed toroidal angle. The results obtained in the toroidal scan for the total currents and the current density profiles, for the same conditions of figure 11, are shown

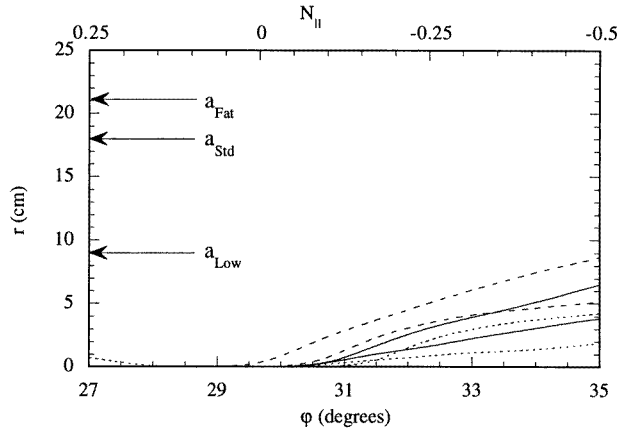


Figure 10. Position where the power deposition profile has its maximum against the toroidal angle, φ , for the std (full curve), fat (broken curve) and low (dotted curve) configurations. The upper curves for each configuration correspond to case 2.

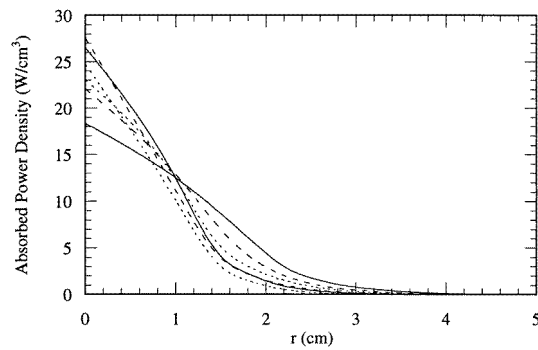


Figure 11. Power deposition profiles for the std (full curve), fat (broken curve) and low (dotted curve) configurations. The broader profiles correspond to case 2. Note that the radius of each configuration is different, see table 1.

in figure 13 and figure 14. The large current obtained for $N_{\parallel} < 0$ is not only due to the dependence on N_{\parallel} but also because of off-axis absorption (see in figure 10 the position where absorption takes place). Note that it is possible to induce rather high currents, in both directions, due to the strong dependence of the magnetic field on the toroidal angle φ , since the dependence of N_{\parallel} on k is very weak (actually the toroidal angle has only varied from 27° to 35°).

A second scan was performed tilting the mirror in the poloidal direction while keeping φ constant. The results of this scan are shown in figures 15 and 16 for the total induced currents, as well as the current density profiles for the maximum induced current.

In both scans it is possible to find a combination of mirror angles such that the induced current is zero. Moreover, since the injection takes place at two stellarator symmetric toroidal angles, the results obtained for the other line are exactly equivalent through a change in the sign of the current. This makes it possible to have not only on- but off-axis heating without inducing currents using an antisymmetric setting for the launching

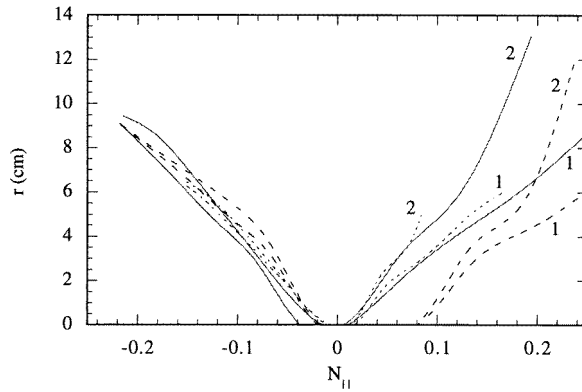


Figure 12. Position where the power deposition profile has its maximum against $N_{||}$, for a fixed toroidal angle, $\varphi \approx 30^\circ$, and the std (full curve), fat (broken curve) and low (dotted curve) configurations.

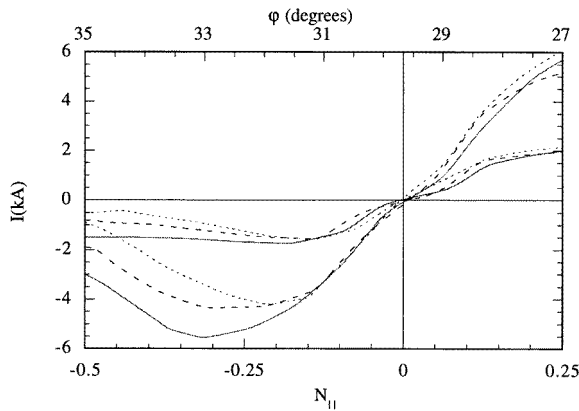


Figure 13. Total induced current by ECCD for a toroidal scan against the mean parallel refractive index, and the std (full curve), fat (broken curve) and low (dotted curve) configurations. Larger currents correspond to case 2.

angles and the same amount of power in both lines, and to control and scale, up to the value appearing in figure 13, the induced current by modifying the injected power in each launching system. Also, comparing figures 12 and 15 it is possible to induce, with only one of the launching systems, localized currents in both directions for the same effective radius, and thus using the appropriate launching settings in both lines, it is possible not only to cancel the current but also to add their contributions.

According to figure 5 the flexibility in the launching conditions can be used to study the possible influence of trapped particles. In table 2 there is a comparison, for the same conditions of figure 16, between the value obtained for the induced current with and without the effect of trapped particles. From this table it is apparent that, as is well known, ECCD efficiency decreases when considering trapped particles. However, it is difficult to relate the reduction of the efficiency to the fraction of trapped particles appearing in figure 5 directly, because the induced current is a complicated convolution relating trapped electrons at different positions both in real and phase space. The capabilities

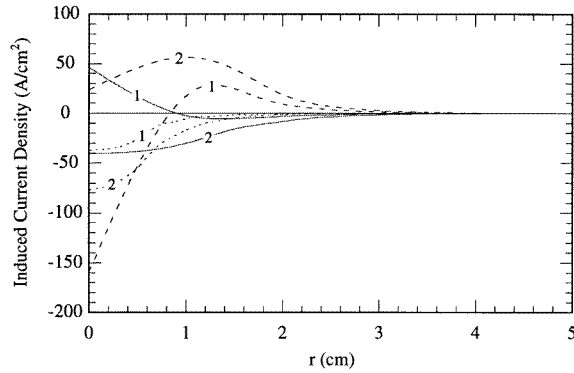


Figure 14. Induced current density profiles for the std (full curve), fat (broken curve) and low (dotted curve) configurations. The total induced currents for each case are: $I_{\text{std}}^1 = 0.004$ kA, $I_{\text{fat}}^1 = -0.0245$ kA, $I_{\text{low}}^1 = -0.059$ kA, $I_{\text{std}}^2 = -0.33$ kA, $I_{\text{fat}}^2 = 0.67$ kA, $I_{\text{low}}^2 = -0.136$ kA. The cases correspond to the conditions of figure 11, with $N_{\parallel} \approx 0$.

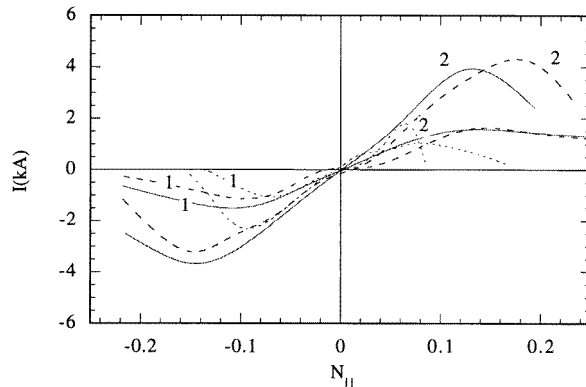


Figure 15. Total induced current by ECCD for a poloidal scan, at $\varphi \approx 30^\circ$, against the mean parallel refractive index, and the std (full curve), fat (broken curve) and low (dotted curve) configurations.

of the designed ECRH system with regard to inducing localized currents can also be used to study the confinement properties of the plasma by modifying the rotational transform profile or magnetohydrodynamic (MHD) stability [12]. To estimate this modification, the free boundary VMEC 3D equilibrium code [13] was used, introducing the current density profiles obtained with the ray tracing code for ECCD. As an example of these calculations, the iota profiles for zero current and two launching conditions, corresponding to case 2 for the standard configuration, are presented in figure 17. ECCD can also be used to locally compensate bootstrap currents. The current density profile of the bootstrap current for TJ-II derived from neoclassical estimations [14] is centred at approximately half radius, and thus the flexibility of the ECRH set up in inducing localized currents by ECCD at different plasma radii and in different directions can be used to at least partially compensate such currents (in fact the highest induced current is obtained near half radius, see figure 16). However, the effect of bootstrap currents on the plasma performance, and the rotational transform ι , of TJ-II is very small [15] since, in the first phase of operation, only ECRH

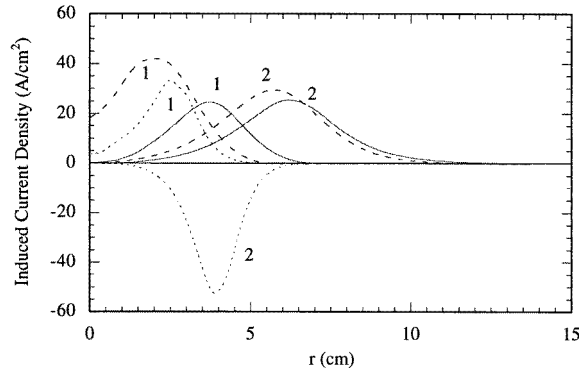


Figure 16. Induced current density profiles for the std (full curve), fat (broken curve) and low (dotted curve) configurations for the conditions of maximum ECCD of figure 15. The integrated current values appear in table 2.

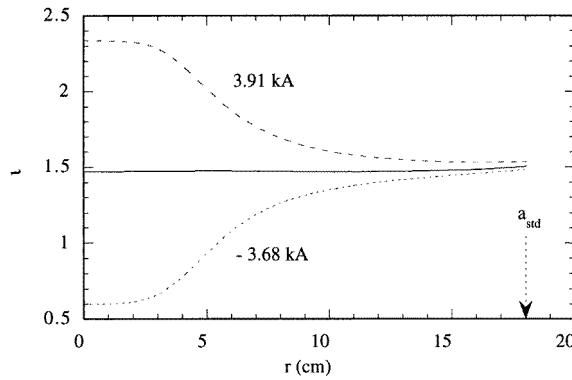


Figure 17. Rotational transform profile for the standard configurations of TJ-II, for zero induced current (full curve), $I = 3.9$ kA ($N_{\parallel} = 0.131$) and $I = -3.68$ kA ($N_{\parallel} = -0.145$). Both cases have the maximum current density at $r_{\text{eff}} = 0.35$.

(cut-off density $\simeq 1.75 \times 10^{19} \text{ m}^{-3}$) will be used for heating. For this reason, in figure 17 the modification of ν due to bootstrap current has not been included.

4. Conclusions

In this paper the ECRH system installed in the TJ-II stellarator is presented and its capabilities within the framework of linear theory is described. The main characteristics of the range of configurations in TJ-II has also been presented along with those specifically related to ECRH and ECCD. Within the geometric optics approximation it is shown that the designed ECRH set up gives full single pass absorption for every magnetic configuration, and moreover localized power deposition both on- and off-axis with the possibility to heat at positions with a different fraction of trapped particles. It is also shown that, with the system as designed, it is possible to induce and control, appreciable localized currents in both directions for the same effective radius, thus opening the possibility to use ECCD to locally control plasma currents and the ν profile. These results are hardly affected by polarization degradation once the optimum launching polarization is chosen.

Acknowledgments

The authors thank F Castejón and A López-Fraguas for fruitful discussions. We would also like to thank the referees for pointing out the problem of the high speed limit approximation for our conditions.

Appendix A. Evolution of the state of polarization

As has been noted in the text one of the points that makes TJ-II different from other fusion devices is its complex magnetic structure. Because of this, even discarding refraction effects, the angle between the incident microwave beam and the local magnetic field varies strongly along the ray trajectory. As it is well known, a component of the magnetic field in the direction of propagation, and shear in the magnetic field can both lead to rotation of the polarization. In an earlier work [2], concerning electron cyclotron emission in TJ-II, one of the reasons for choosing the line of sight was precisely to minimize both effects (Faraday rotation and magnetic field shear). In that work it was checked that the effect was small. However, the flexibility requisites imposed on the designed ECRH set up needs a general treatment, given in this appendix.

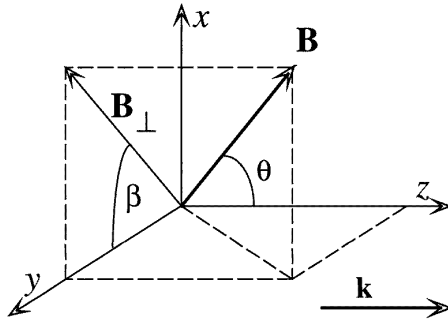


Figure A1. Coordinate system used for calculations.

The evolution of the state of polarization in a magnetized plasma has been studied by some authors in connection with ionospheric propagation [16] and magnetic field determination in tokamaks [17, 18]. To compute the evolution of the polarization of an electromagnetic wave with frequency near, or equal, to the electron cyclotron frequency or its harmonics in a magnetically confined plasma we will follow the formalism used in [17]; in which the state of polarization is uniquely represented by a point $s = \{s_1, s_2, s_3\}$

$$s_1 = \cos 2\chi \cos 2\psi \quad s_2 = \cos 2\chi \sin 2\psi \quad s_3 = \sin 2\chi \quad (\text{A.1})$$

with $(-\pi/4 \leq \chi \leq \pi/4, 0 \leq \psi \leq \pi)$ in the *Poincaré sphere*, and where its evolution is obtained by a rotation about an axis passing through the characteristic polarizations. This formalism, originally employed in crystal optics [19], has an advantage over the coupled first- and second-order formalism: it is not limited to vanishingly small shear, and moreover it naturally includes the Faraday rotation effect. Although the underlying theory is only valid for uniform media it can be readily extended to the non-uniform case if the spatial variation of the plasma parameters is small compared to the radiation wavelength, so that the WKB solution of Maxwell equations holds. Therefore, we will regard the characteristic waves and refractive indexes to be constant in a narrow slab dl although they are allowed to change

from one infinitesimal slab to the next. Thus, in the WKB approximation the change in the state of polarization along the beam path inside the plasma (parametrized by the variable l) is simply an infinitesimal rotation about an axis, defined by the fast characteristic polarization s_f , of an angle Ω , equal to the phase difference between the two characteristic polarizations

$$\frac{ds(l)}{dl} = \Omega(l) \times s(l) \quad (\text{A.2})$$

where $\Omega(l) = \omega/c|N_O(l) - N_X(l)| s_f(l)$ and N_O and N_X are the refractive indexes corresponding to the O and X modes. By integrating equation (A.2) one may obtain the state of polarization at any point along the ray path for a given initial polarization s_0 when the local polarization of the fast wave s_f and the refractive indexes are known. Since the coordinates of the point s in the *Poincaré sphere* are the *Stokes parameters*, these can readily be obtained from the cold dispersion equation for the electric field of the wave. Using the co-ordinate system shown in figure A1 and after a tedious calculation they are found to be

$$s_f(l) = \frac{\{\cos 2\beta(l), \sin 2\beta(l), F(l)\}}{\sqrt{1 + F^2(l)}} \quad F(l) = \frac{2(1 - \omega_p^2(l)/\omega^2) \cos \theta(l)}{\omega_c/\omega \sin^2 \theta(l)} \quad (\text{A.3})$$

where (cf equation (A.1)) $\chi = 1/2 \arctan F$ and $\psi = \beta$, being ω_p and ω_c the plasma and electron cyclotron frequencies, respectively. The absorption of ECRH waves, in a given mode of polarization, has to be computed taking into account that the calculated local absorption coefficient must be multiplied by the fraction of the injected power in that mode. For a wave with power P_0 , launched in a polarization state s_0 , the state of polarization, at a given point l along the ray path, $s(\chi(l), \psi(l))$ is computed by integrating equation (A.2) and the fraction of the power in the local polarization state s_X (or s_O), at this point is [19]

$$P_{X,O} = \frac{P_0}{2} [\sin 2\chi_s \sin 2\chi_{X,O} + \cos 2\chi_s \cos 2\chi_{X,O} \cos(2\psi_s - 2\psi_{X,O})]. \quad (\text{A.4})$$

Solving equation (A.2) for an initial launching polarization, and evaluating equation (A.4) along the ray trajectories it is possible to obtain the fraction of power in a given mode of propagation. These features have been added to the TRECE [2] ray tracing code. Extensive simulations have been performed for different configurations, launching directions, and densities for TJ-II using as initial polarization for launching the one corresponding to the X-mode at the position of the maximum power deposition, i.e. discarding the possible modification of the polarization from the launching to the absorbing region. The main result of this study is that, because of the evolution of polarization inside the plasma, up to 15% of the launched power has O-mode polarization in the resonant region. This result raises the question whether it is possible to use the tools included in the code to obtain a better initial launching polarization. Using the fact that in the framework of geometrical optics the ray trajectories are reversible, a procedure consisting in two steps have been used to obtain the launching polarization. First, the central ray defining the beam is traced from the launching system to the plasma, integrating the ray equations, and its power deposition profile computed for a given mode of polarization (O or X). In the second step equation (A.2) is integrated from the resonant region to the launching system, along the reversed trajectory, using as initial polarization, s_0 , the local value corresponding to the desired mode. The polarization obtained from equation (A.2) at the point where the ray exits the plasma is precisely the one that should be used for launching, because its evolution inside the plasma is such that has the desired polarization state (O or X) in the resonant region.

As an example of this effect, the fraction of power, in the X-mode (cf equation (A.4)), along the ray arclength is plotted in figure A2 for the conditions of case 2 of figure 11 and two

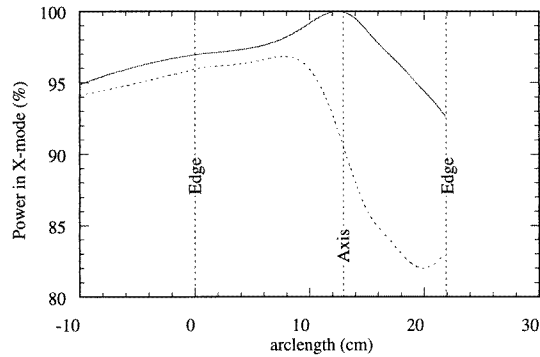


Figure A2. Local fraction of power in the X-mode for the line QTL1 against the central ray arclength, for the initial optimum polarization $s = \{-0.197, -0.928, -0.341\}$ (full curve) and the initial polarization corresponding to a pure X-mode at the axis $s = \{0.213, -0.978, 0.085\}$ (dotted curve).

initial polarizations: the polarization corresponding to a pure X-mode in the resonant region, and the polarization as obtained from the optimization procedure. It is worth mentioning that the optimum polarization is different for different magnetic configurations, launching conditions and densities. This approach to computing the optimum polarization can only be regarded as a zeroth order approximation to complete optimization; on the one hand the optimization for Gaussian beams requires an optimization that depends on the wavefront shape, because of the electric field mode structure of these beams; and on the other hand wave scattering due to density fluctuations in the plasma edge can also lead to polarization scrambling.

References

- [1] Alejaldre C et al 1988 *Fusion Technol.* **13** 521
- [2] Tribaldos V and Van Milligen B Ph 1996 *Nucl. Fusion* **36** 283
- [3] Guasp J and Liniers M 1997 Dependencia de las regiones de atrapamiento con el campo electrico radial en el TJ-II *CIEMAT Rep.* **824**
- [4] Rome M et al 1997 *Plasma Phys. Control. Fusion* **39** 117
- [5] Sorolla M et al 1997 *Int. J. Infrared Millimeter Waves* **18** 1161
- [6] Alejaldre C and Guasp J 1987 *Nucl. Fusion* **27** 2153
Alejaldre C and Castejon F 1989 *Phys. Fluids B* **1** 2201
Castejon F, Alejaldre C and Coarasa J A 1992 *Phys. Fluids B* **4** 3689
- [7] Fisch N J 1987 *Rev. Mod. Phys.* **59** 175
- [8] Karney C F F and Fisch N J 1986 *Phys. Fluids* **29** 180
- [9] Tribaldos V and Van Milligen B Ph 1997 *Rev. Sci. Instrum.* **68** 931
- [10] Mazzucato E 1989 *Phys. Fluids B* **1** 1855
Nowak S and Orefice A 1994 *Phys. Plasmas* **1** 1242
- [11] Yariv A 1989 *Quantum Electronics* (New York: Wiley)
- [12] Renner H et al 1989 *Plasma Phys. Control. Fusion* **31** 1579
- [13] Hirshman S P, Van Rij W I and Merkel P 1986 *Comput. Phys. Commun.* **43** 143
- [14] Rodriguez-Yunta A, Van Rij W I and Hirshman S P 1990 *Proc. 17th EPS Conf. on Controlled Nuclear Fusion and Plasma Physics (Amsterdam 1990)* vol 14B, part 2, p 505
- [15] Rodriguez-Yunta A 1991 *Proc. 8th Int. Workshop on Stellarators, IAEA Technical Committee Meeting (Kharkov USSR)* p 69
- [16] Budden K G 1964 *Principles of Optics* (Oxford: Pergamon)
- [17] De Marco F and Segre S E 1972 *Plasma Phys.* **14** 245
- [18] Fidone I and Granata G 1971 *Nucl. Fusion* **11** 133
- [19] Ramchandran G N and Ramaseshan S 1961 *Crystal Optics, Encyclopedia of Physics* **25** (Berlin: Springer)